SHORT RANGE ORDER STRUCTRURES OF LITHIUM OXY-THIOSILICOPHOSPHATE GLASSES

Guantai Hu, Victor M. Torres III, Steve W. Martin*

Department of Materials Science and Engineering Iowa State University of Science & Technology Ames, Iowa, 50011, United States

Abstract

In this work, the compositional series of sulfide and mixed oxysulfide (MOS) glasses 0.56Li₂S + $0.44[(0.33-x)PS_{5/2} + xPO_{5/2} + 0.67SiS_2]$ was prepared, where $0 \le x \le 0.33$, and their short range order (SRO) structures and their thermal properties have been investigated. Powder x-ray diffraction (XRD) confirmed that the MOS glasses were free from crystallization, with only very minor diffraction peaks in the x = 0 glass being observed. Fourier transform infrared (FT-IR), Raman, and ²⁹Si and ³¹P magic angle spinning (MAS) NMR spectroscopies were used to identify the SRO structures present in these glasses. These spectra revealed oxygen migration from P to Si during synthesis. Although oxygen was introduced in the form of phosphorus oxide, the majority of the oxygen in these glasses ends up being bonded to silicon, thereby creating sulfur-rich SROs centered by phosphorus and MOS SROs centered by silicon. It was further found that the P-S SRO species were predominantly charged non-bridging sulfurs (NBS). The Si SRO species were comprised of neutral bridging oxygens (BOs) and charged non-bridging oxygens (NBOs) and neutral bridging sulfurs (BS) and charged non-bridging sulfurs with the neutral BO and BS species being larger in fraction than the NBO and NBS. These results suggest that the preponderance of the mobile Li⁺ cations in these glasses are located near the more negatively charged P centers and not near the more neutrally charged Si centers. The average negative charge of the P SRO structures was found to be \sim -3.0 with \sim 97% of the phosphorous species in the P⁰ SRO while the average negative charge of the Si SRO structures was found to

be -2.3. Consistent with the creation of the large numbers of NBS on the P and more BOs and BSs on the Si, these values are more negative and more positive, respectively, than the compositionally expected average value of -2.55. Differential scanning calorimetry (DSC) measurements of their glass transition (Tg) and crystallization (Tc) temperatures showed that the Tgs of these glasses are higher than 300°C and their working ranges, $\Delta T \equiv Tc - Tg$, are ~ 100°C. **Keywords**: MOS glass, sulfide glass, SRO structure, Raman, FT-IR, MAS NMR

1. Introduction

Lithium-ion conducting glasses have been studied for more than 40 years with the goal of developing them as solid electrolytes (SEs) in secondary batteries. Lithium-ion batteries (LIBs) have been widely accepted and applied in various energy storage applications due to their good energy and power densities, and cycling capability. [1, 2] However, safety concerns due to the use of volatile and flammable organic liquid electrolytes (OLEs) still remain. For this reason, SEs, owing to their higher thermal stability, are being considered as safer alternatives in next generation LIB applications. [3] Further, the fully dense structure of the glassy solid electrolytes (GSEs) and their lack of grain boundaries can potentially reduce the formation, growth, and subsequent electrolyte penetration of lithium dendrites. [4], [5] For these reasons, among various kinds of SEs studied globally, GSEs are one of the more promising potential candidates.

Reports on lithium ion conducting sulfide GSEs have been published since the 1980's, due to their superior ionic conductivity over oxide GSEs. [6-17] Researchers have explored a number of sulfide glass and glass-ceramic material families, such as $\text{Li}_2\text{S} + \text{P}_2\text{S}_5$, $\text{Li}_2\text{S} + \text{SiS}_2$, $\text{Li}_2\text{S} + \text{GeS}_2$, $\text{Li}_2\text{S} + \text{B}_2\text{S}_3$ and etc., which have much improved lithium ion conductivities over their oxide glass analogs. [6, 7, 18-24] However, the increased conductivity of sulfide GSEs is

accompanied by their decreased chemical stabilities against air and lithium metal. These latter two characteristics require high quality oxygen- and water-free synthesis environments and generate poor electrochemical performance when used with high energy lithium metal anodes, respectively.

Motivated to improve the chemical stability of pure sulfide GSEs, GSE compositions have been doped with oxygen as a method to achieve this goal. [25-28] For instance, lithium-oxysalts, such as Li₄SiO₄ or Li₃PO₄, have been added to Li₂S + SiS₂ GSEs. It was found that with a small amount of oxysalts, approximately 5 mole %, introduced into the composition, higher stability has been achieved with comparable or even slightly increased ionic conductivities. [26, 28-31] Studies of these MOS GSEs have also been expanded to other glass systems and similar results have been observed. [32-35] Therefore, this oxygen-doping strategy has been considered as an effective way to find better GSE candidates from the pure all-sulfide GSEs.

In addition, mixing two glass forming elements, such as silicon, phosphorus, boron, germanium etc., has also been considered as a method of yielding better GSEs. A previous study on the $\text{Li}_2\text{S} + \text{SiS}_2 + \text{GeS}_2$ system, for example, has shown that the ionic conductivities of mixed-glass-former (MGF) glasses were two orders of magnitude higher than the base binary GSEs $\text{Li}_2\text{S} + \text{SiS}_2$ or $\text{Li}_2\text{S} + \text{GeS}_2$, with the same Li_2S content. [36] By incorporating Ga_2S_3 into $\text{Li}_2\text{S} + \text{GeS}_2$ glasses, up to Ga / (Ge + Ga) = 0.25, the glass transition temperature (Tg) and ionic conductivity increased with the addition of Ga_2S_3 . [37, 38] Also, it has been found that adding P_2S_5 to $\text{Li}_2\text{S} + \text{SiS}_2 + \text{LiI}$ can improve electrochemical stability in contact with lithium metal, also the GSE exhibited a very high ionic conductivity of 2 mS/cm at room temperature. [39]

Based upon these results, two glass formers, silicon and phosphorus, are used in the glass system in this study here. Silicon and phosphorus are both cheap and abundant elements and are also both good glass formers, while yet having slightly different and complimenting advantages. Thiosilicate GSEs have low vapor pressures, but have higher melting temperatures. [23] Thiophosphate GSEs, on the other hand, have higher vapor pressures, but lower melting temperatures. [40] In this work, we have combined silicon and phosphorus glass formers to reduce the melting temperatures while still having lower vapor pressure liquids. This latter attribute enables the use of open crucibles instead of sealed vitreous quartz ampoules for synthesis, leading to significantly reduced working complexity and cost.

In other GSEs systems, mixed glass formers (MGFs) can exhibit a positive impact on several properties especially the ionic conductivity. [36, 41] For this reason, the compositions in this work combine phosphorus and silicon to capitalize upon the positive influence of the mixed glass former effect (MGFE) and lead to a promising compositions for SE applications. Finally, to take advantage of the MOS effect on the properties of GSEs, we have systematically added oxygen to the base pure sulfide GSE to explore in more detail the effects on the structure and properties of the MOS GSEs.

To have a good insight into the potential applications of these GSEs, it is crucial to investigate the atomic level structures and the chemical bonding environments in these GSEs. Understanding the local bonding environments in these GSEs can inform researchers of the atomic topologies in these GSEs that can aid in the explanation of why these GSEs behave differently when used as SEs in comparison to other SEs.

In the past, only a limited number of reports have been made of MGF MOS GSEs and little structural information has been discussed about them. For example, Li₂S + SiS₂ GSEs have

been reported to have enhanced ionic conductivity when doped with Li_3MO_3 (M = B, Al, Ga and In) or ortho-oxide salts, Li_xMO_y (M = Si, P, Ge), in which x = 3 or 4 and y = 4. [29-31] However, these studies have found that these compositions are poor glass formers requiring very fast quenching, > 100 K/sec, and as such these particular oxide salt doped MGF MOS GSEs are difficult to process as bulk monolithic glass pieces. As a result of this, it is really only possible to obtain these particular GSEs as fine powders and the electrochemical tests using glass powder pellets will be dominated by the inter-grain boundaries between all of the powder particles.

Therefore, in this study, efforts have been made to develop a GSE system that can be synthesized via the traditional melt-quench (MQ) method to yield bulk slow quenched samples of thick, t > 1 mm, monolithic glass pieces. The MQ MGF MOS GSEs in the series, $0.56Li_2S + 0.44[(0.33-x)PS_{5/2} + xPO_{5/2} + 0.67SiS_2]$, where $0 \le x \le 0.33$, have been investigated by employing a number of spectroscopic techniques to determine their atomic level structures. These highly modified GSEs have an R-value (ratio of modifier to glass former) = Li/(Si+P) = 2.55 to maintain high ionic conductivity, which will be reported in further publications. Note that $PS_{5/2}$ and $PO_{5/2}$ formula units are used instead of P_2S_5 and P_2O_5 so that the sum of the glass formers is 1. This will simplify developing the chemical models of the structures of these MGF MOS GSEs which might already be considered complicated enough. [42]

DSC measurements of the GSEs Tg and crystallization (Tc) temperatures have been conducted to determine their thermal stability and capability for further processing. Fourier transformation infrared (FT-IR), Raman, and ²⁹Si and ³¹P magic angle spinning nuclear magnetic resonance (MAS NMR) spectroscopies have been carried out to ascertain the types and relative fractions of the various SRO structures present. Powder x-ray diffraction has been conducted as

well to confirm the presence of any contaminating polycrystalline phases as a function of the addition of oxygen into the base pure sulfide GSE.

In summary, these measurements showed that most of the oxygen added in these GSEs, while originally bonded to the starting material PO_{5/2}, was observed to migrate to and become bonded to silicon in the GSEs, with little evidence of residual P-O bonds. Further, the a good fraction of the added oxygen was found to be in bridging oxygen (BO) sites in the form of neutral \equiv Si-O-Si \equiv bonds. Since the Li⁺ charge must be conserved in these GSEs, 2.55Li⁺/ (0.67Si + 0.33P), these neutral BOs sites on Si must be accounted for by increased negative charges on the sulfur atoms bonded to P in the form of non-bridging sulfurs (NBS) in the form of Li⁺ ·S-P \equiv . These NBS on the P centers in turn leads to the formation of depolymerized phosphorus sulfide SRO structures of the type Pⁿ, where n is the number of bridging sulfurs (BS) and is either a 0 or 1.

2. Experimental Methods

2.1 Sample Preparation

Lithium sulfide (Li₂S, 99.9% metal basis, Alfa Aesar), phosphorus pentasulfide (P_2S_5 , 99.95% Sigma Aldrich), phosphorus pentoxide (P_2O_5 , 99.95% Fisher Scientific), and silicon disulfide (SiS₂) were used to synthesize the 0.56Li₂S + 0.44[(0.33-x)PS_{5/2} + xPO_{5/2} + 0.67SiS₂] GSEs. All these materials were commercially purchased except SiS₂ which was prepared in house.

SiS₂ was made by reacting elemental crystalline silicon powder (Si, metal basis, Alfa Aesar) and an excess of elemental sulfur (S, 99.9995% metal basis, Alfa Aesar). Silicon and sulfur were mixed via mechanical ball milling and the resulting powder was then placed into a silica quartz ampoule. The ampoule was then evacuated under vacuum, sealed, and placed into rotatable reaction chamber that was placed inside a tube furnace and rotated at a 15° angle. The

ampoule was then heated from 50 to 970 °C at a rate of 1 °C/min over a period of 52 h and then slow cooled to room temperature. The chamber was kept rotating throughout the heating and cooling steps, ensuring a sufficient dynamic contact between unreacted silicon and liquid sulfur. After being cooled to room temperature, the S + SiS₂ mass was heated in a vertical tube furnace for 8 h at 675 °C with the S + SiS₂ mass situated in the hot zone of the furnace and the opposite end of the quartz ampoule located outside of the furnace and air cooled. A hot-to-cold temperature profile was created in the ampoule allowing for excess S to be distilled off the SiS₂. The SiS₂ was then removed from the ampoule inside a N₂ glovebox.

P₂S₅ and P₂O₅ were used as received as they are very high purity, 99.99 % metals basis, and cannot be easily further purified. The Li₂S and SiS₂ were, however, heat treated at 700°C for 30 mins in a tube furnace attached to a N₂ filled glovebox prior to using in the batch, which we found released surface adsorbed contaminants such -OH and -SH.

These mixed raw materials were batched into 5-gram charges and were then mechanically ball milled for 5 minutes. The mixture was then melted in a vitreous carbon crucible between 850 to 950°C for 5 minutes, using a tube furnace attached hermetically to a N₂ filled glovebox. After the first melt, weight of the room temperature melted composition was measured and the weight loss was determined. Less than 2% weight loss was observed for all of the glass compositions. Samples were then melted again for 5 minutes and splat quenched to the glassy state between thick brass plates in thicknesses of about 1 mm.

2.2 Differential Scanning Calorimetry (DSC)

Differential scanning calorimetry (DSC) measurements were performed using a calibrated (± 2 °C) Perkin Elmer Diamond DSC to determine the Tgs and Tcs. Here, ~ 20 mg glass pieces were hermetically sealed in aluminum pans inside a N₂ filled glovebox and

transferred to the DSC. An initial set of DSC survey experiments, scanned at a rate of 20°C/min. from 50 to 450°C, were used to locate the Tg and Tc for each sample. With both Tg and Tc so determined for each sample, an additional set of DSC cycle experiments were performed. The initial scan started at 50°C and heated up to ~20 °C beyond the Tg but below the Tc, as determined from the initial DSC thermogram. Further scans were then performed by cooling from this initial upper temperate limit down to 200°C followed by reheating to ~20°C beyond the Tg, but below the Tc, three times to relax the glass structure and obtain more reliable Tg values that were independent of the initial MQ cooling rate. A final heating scan was measured from 200° to 450°C to determine both Tg and Tc values after the cycle scans. Tg and Tc values reported here were taken as averages of the three Tgs and the single value of Tc. These DSC measurements were made in triplicate and all values of Tg and Tc so determined were averaged. The sample errors were taken as the standard deviation of all of these measurements on these three samples.

2.3 Powder X-ray Diffraction (XRD)

Powder x-ray diffraction experiments were conducted using a Rigaku SmartLab x-ray diffractometer with a copper anode under 40 kV voltage and 44 mA current. Two-theta signals were collected from 10 to 70° in 0.01° steps at 1° per minute. The GSEs were ground into fine powder with an agate mortar and pestle and then sealed inside an air-tight sample holder on top of a zero-background silicon wafer.

2.4 Raman Spectroscopy

Raman spectra were collected on a JASCO NRS-3100 laser Raman spectrophotometer using a 150mW 785nm laser. Scans were done from 160 to 1890 cm⁻¹ on glass flakes. Materials were sealed in an airtight sample holder to prevent air exposure.

2.5 Fourier-Transform Infrared Spectroscopy (FT-IR)

The Mid-IR spectra were collected with a Bruker IFS 66v/s FT-IR spectrometer. Samples were ground with dry CsI using a weight ratio of 1 GSE : 40 CsI in an agate mortar and pestle inside a N_2 -filled glovebox. 0.2000 ± 0.0010 g of the mixed powders was then pressed in a die forming a uniform and optically translucent pellet. CsI background pellets were produced in the same way, but with only 0.2000 ± 0.0010 g of dry CsI. Spectra were collected in transmission through these two sets of pellets from 400 to 4000 cm⁻¹ using a KBr beam splitter and 32 scans at a resolution of 4 cm⁻¹.

2.6 ³¹P and ²⁹Si Magic-Angle-Spinning (MAS) Nuclear Magnetic Resonance (NMR) Spectroscopy

600 MHz and 400 MHz spectrometers were used to collect the ³¹P and ²⁹Si MAS NMR spectra, respectively. The GSEs samples were densely packed into a spin rotor and spun at 12 kHz at the magic angle to the magnetic field. For ³¹P NMR, 80 scans were done for each sample with a delay of 5 minutes between scans. For ²⁹Si NMR, a 12 kHz spinning rate was used and data was collected with 3658 scans and delayed by 45 to 300 seconds between scans. The spectra were analyzed using the NMR spectra analysis software DMFit.[43]

3. Results

3.1 Differential Scanning Calorimetry

Figure 1 shows the full DSC thermograms for all the glasses in the $0.56\text{Li}_2\text{S}$ + $0.44[(0.33-x)PS_{5/2} + xPO_{5/2} + 0.67SiS_2]$ glass series from x = 0 to x = 0.33 for the final heating step of the DSC cycle scan at 20°C/min for all compositions. The Tg and Tc were determined as shown in figure as the onset of the glass transition and crystallization processes, respectively. As shown in **Fig. 2A**, Tg increases from 292 to 324 °C as x increases from 0 to 0.25 and then decreases to 315°C for the x = 0.33 GSE. This result is consistent with the stronger P-O bonds

introduced into the glass structure compared to the weaker P-S bonds. **Figure 1** shows that there is only one strong crystallization peak observed for all MOS GSEs, whereas the pure sulfide glass, x = 0, exhibited two crystallization peaks. The Tc onset temperatures of the first crystallization peaks of the pure sulfide and MOS GSEs are shown in **Fig. 2B.** Tc values for these GSEs increase in two steps, first from 384 °C to 407 °C with x changing from 0 to 0.083 and then from 405 °C to 414 °C with x changing from 0.25 to 0.33. The working range, $\Delta T = Tc$ – Tg, is plotted in **Fig. 2C**, and shows that the ΔT for all the GSEs in this composition series are ~ 100 °C ± 10 °C. We have chosen this particular definition of the working range because in future work these GSEs will be subjected to viscous deformation processing above the Tg of the glass but below the Tc of the supercooled liquid. The working range so defined here provides a good estimate of the temperature range over which such viscous deformation processing into thin films, 10 to 200 micron thick, will be possible.

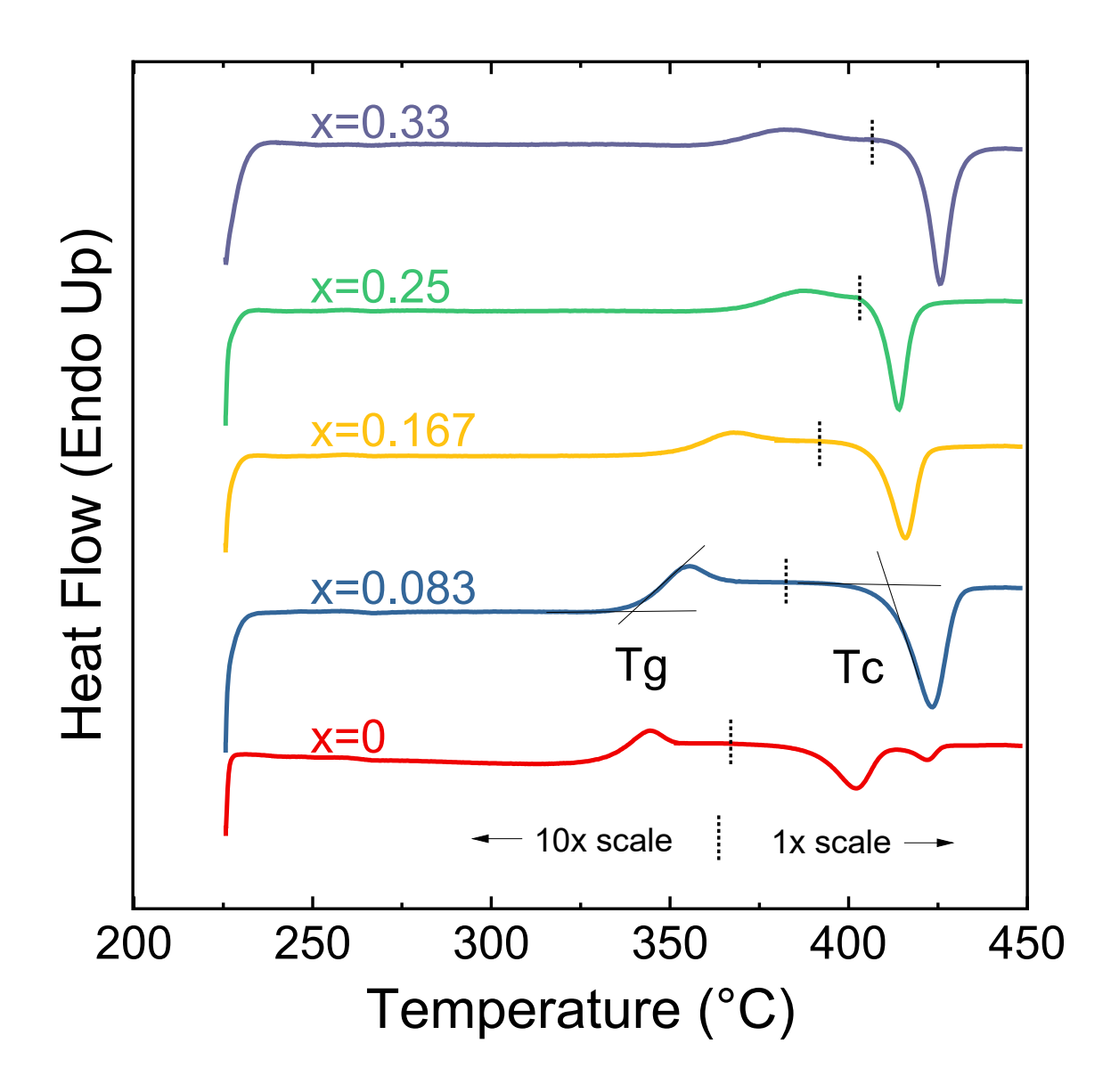


Fig. 1. Final heating step of the cycling DSC experiments for $0.56\text{Li}_2\text{S} + 0.44[(0.33\text{-x}) \text{PS}_{5/2} + \text{xPO}_{5/2} + 0.67\text{SiS}_2]$ GSEs, x = 0, 0.083, 0.167, 0.25, 0.33 from 225°C to 450°C . Tg and Tc values were determined as onset values of the glass transition and crystallization processes as shown in the construction. The vertical dotted lines on the graphs show the temperature ranges where the scale is 10x magnified, to lower temperatures, to clearly show the glass transition phenomena and where the scale is not magnified, 1x, to higher temperatures, to show the much stronger exothermic crystallization phenomena.

Figure 2A shows that with increasing oxygen concentration, the Tgs tend to increase and this is consistent with the stronger bonding and field strength that oxygen provides to the glass structure, requiring higher thermal energy to access the viscous relaxation modes of the

supercooled liquid state above the Tg of the glass. However, when oxygen is maximized in this series, for the x = 0.33 GSE, the Tg goes decreases, which may be related to the change from the two phosphorus sources, P_2S_5 and P_2O_5 , to a single P_2O_5 source as the raw material and the formation of more ionic SRO structures that have fewer network bonding structures. This will be examined below in the spectroscopic studies of the structure of these GSEs.

From Fig. 2B, it is also clear that Tc is also related to the amount of oxygen substituted into these GSEs. From x = 0 to x = 0.33, Tc increases from 384°C to 414 °C, a trend that is consistent with the Tg data. The Tgs are > 290 °C and this enables these GSEs to accommodate much wider temperature ranges over which they can be used, if required, than the traditional OLEs. The working range, ΔT , shown in Fig. 2C, on the other hand, does not show a clear compositional dependence. Rather, it is ~100 °C ±10 °C for all of the glasses. We have observed that a GSE with a ΔT value of at least 100 °C is often sufficiently stable against crystallization to enable the GSE to be heated and then drawn into a thin film without detrimental crystallization events.

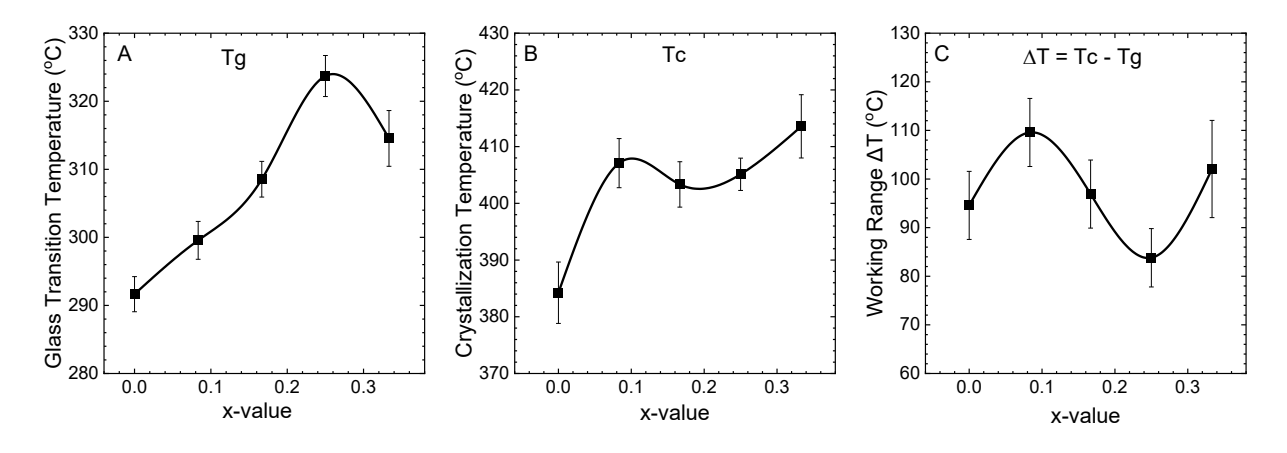


Fig. 2. (A) Glass transition temperature Tg, (B) onset crystallization temperature Tc, and (C) working range $\Delta T = Tc - Tg$ of $0.56Li_2S + 0.44[(0.33-x)PS_{5/2} + xPO_{5/2} + 0.67SiS_2]$ GSEs, x = 0, 0.083, 0.167, 0.25, 0.33. The lines through the data points are shown only as guides to the eye and have no other significance.

3.2 Powder X-ray Diffraction

Powder x-ray diffraction has been used to determine the presence of crystalline phases in these GSEs. As seen in **Fig. 3**, all the MOS GSEs have smooth, essentially featureless curves across the range of 10 to 70° without any peaks, indicating these GSEs are fully x-ray amorphous. However, on very close inspection, for the pure sulfide GSE with x = 0, very low intensity peaks corresponding to Li₄SiS₄ are observed, suggesting that a small amount of Li₄SiS₄ crystal has precipitated out from the glass melt during cooling. This suggests that one of the crystallization peaks in the DSC scan maybe associated with Li₄SiS₄. However, this peak in the XRD pattern is very weak and suggests that the crystalline Li₄SiS₄ phase is a very small fraction of the volume of the x = 0 GSE.

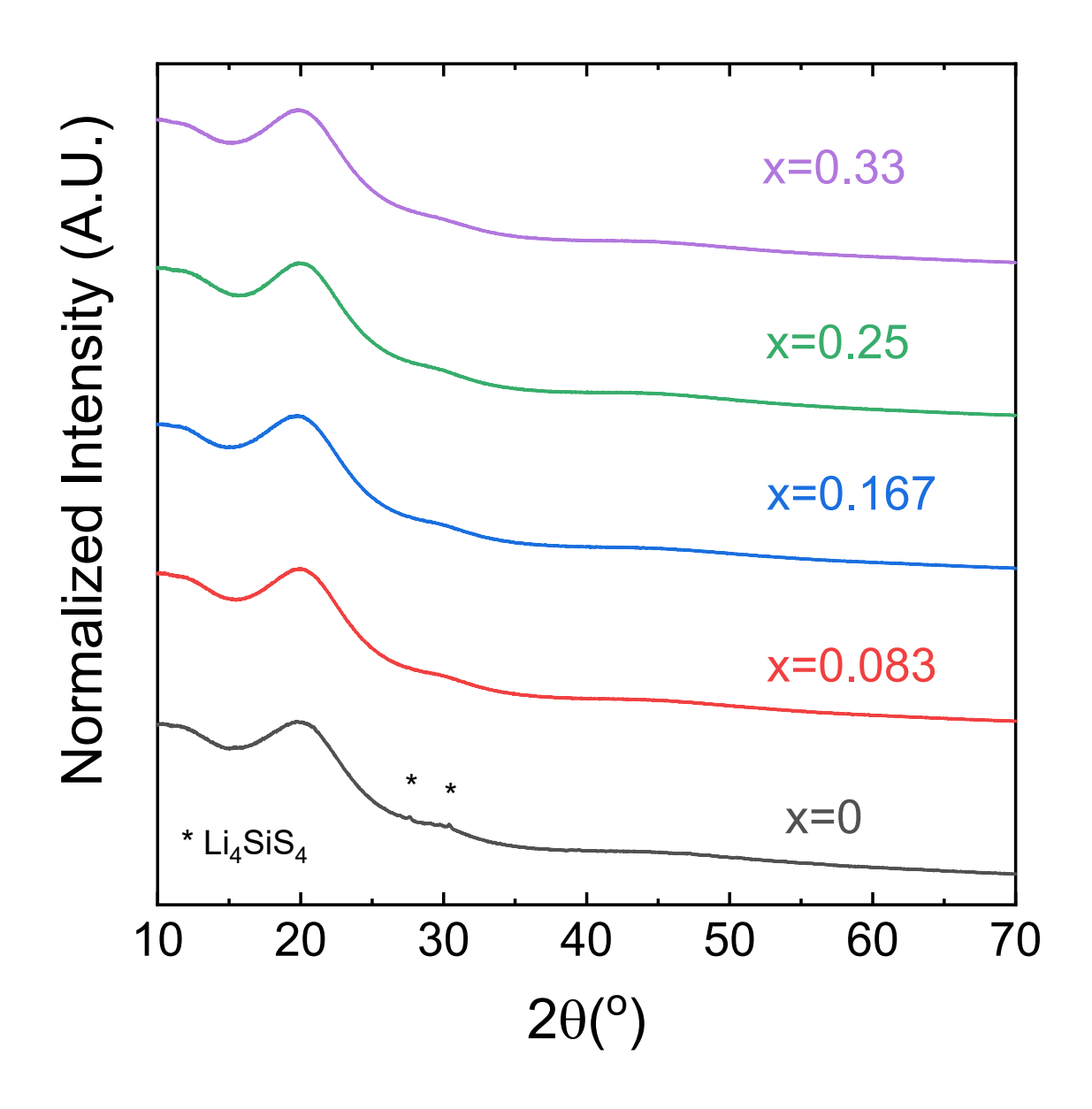


Fig. 3. Powder x-ray diffraction patterns of $0.56\text{Li}_2\text{S}+0.44[(0.33-x)\text{PS}_{5/2}+x\text{PO}_{5/2}+0.67\text{SiS}_2]$ GSEs, x = 0, 0.083, 0.167, 0.25, 0.33.

3.3 Raman Spectra

The Raman spectra of the GSEs in the $0.56\text{Li}_2\text{S} + 0.44[(0.33-x)\text{PS}_{5/2} + x\text{PO}_{5/2} + 0.67\text{SiS}_2]$ glass series are shown in **Fig. 4**. In the high wavenumber range, >800 cm⁻¹, of the spectra, very weak bands are observed and are assigned to the formation of P-O and Si-O species. Note that

the y-axis scale has been multiplied by a factor of 10 in this region to be able to see these weak features more clearly. The significantly lower scattering intensity is due to the much smaller polarizability of P-O and Si-O bonds compared to P-S and Si-S bonds, and as a result these peaks are much lower intensity compared to peaks arising from the more polarizable P-S and Si-S bonds.[44] For this reason, the high wavenumber region has a 10x expanded y-axis in **Fig. 4A** and shows that a single high frequency mode at 1,400 cm⁻¹ grows in with added PO_{5/2}. This peak is associated with the P=O vibration of the P³ SRO group. This assignment will be more carefully analyzed below where the ³¹P and ²⁹ Si MAS NMR spectra are analyzed.

In addition to these weaker peaks above 800 cm^{-1} , **Fig. 4A** shows that the most significant Raman bands reside in the region between $200 \text{ and } 800 \text{ cm}^{-1}$. These lower wavenumber resonances arise from highly polarizable sulfide related SRO structures, hence the higher signal strength compared to the oxide peaks. The peak centered at 423 cm^{-1} is actually two superimposed peaks of essentially the same frequency and are assigned to the symmetric vibration of non-bridging sulfurs (NBS) in sulfide $\text{Si}_2\text{So}_4^{-1}$ (called E^1Si^2) and PS_4^{-3} (called P^0) SRO units. [18, 20, 45] In this notation, the superscript n on P or Si refers to the total number of bridging bonds on the Si and P atoms, n = #BS + #BO. The shoulder at 386 cm^{-1} has been assigned to the symmetric vibration of NBS in $\text{P}_2\text{So}_4^{-1}$ (P^1P) and SiS_4^{-1} (Si^0) SRO units. [20, 44, 46-49] The P^1P SRO is a P^1 SRO unit where the bridging bond is a direct P-P bond and the BS between the two P atoms has been lost. For this reason, this structure is often called a defect structure owing to the missing S in the first coordination sphere.[50]

Across the glass series, from x = 0 to x = 0.33, this shoulder decreases in intensity and this suggests that introducing oxygen decreases the presence of the defect P^{1P} and molecular anion Si^0 structures in these GSEs. This observation agrees well with the ^{31}P and ^{29}Si MAS NMR

spectra that will be discussed below. The broad low intensity peak at 562 cm⁻¹ is assigned to the v_3 degeneracy mode (F₂) of the PS₄³⁻ P⁰ SRO unit. [51]

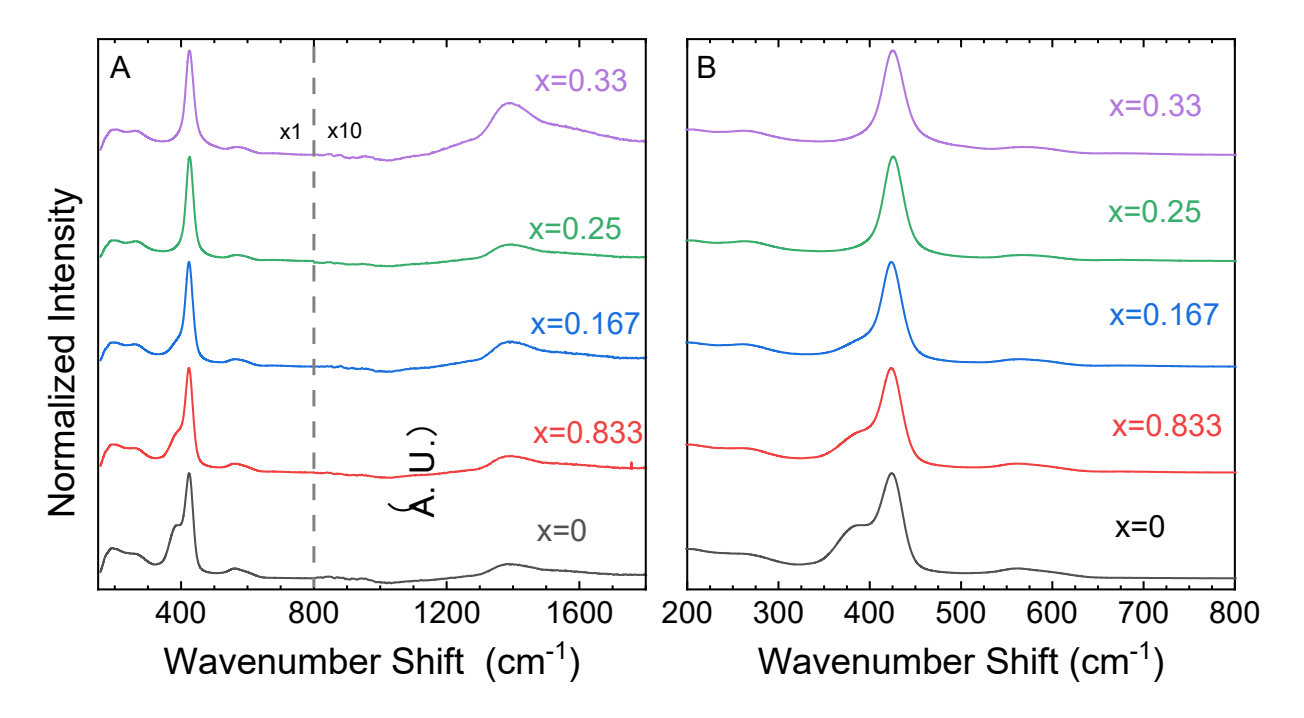


Fig. 4. (A) Full and (B) low wavenumber Raman spectra of $0.56\text{Li}_2\text{S}+0.44[(0.33-x)\text{ PS}_{5/2}+x\text{PO}_{5/2}+0.67\text{ SiS}_2]\text{ GSEs}, x = 0, 0.083, 0.167, 0.25, 0.33. Note that in (A) the vertical axis of the high wavenumber region has been multiplied by 10x to better see the weak Raman modes due to P-O and Si-O bonds in these GSEs.$

3.4 Infrared Spectra

As shown in **Fig. 5**, the Mid-IR spectra of the $0.56\text{Li}_2\text{S} + 0.44[(0.33-x)PS_{5/2} + xPO_{5/2} + 0.67\text{SiS}_2]$ GSE series reveals additional structural information which was not revealed in the analysis of the Raman spectra.[44] As expected for the x = 0 glass, there are very weak peaks in the high wavenumber range, $> 800 \text{ cm}^{-1}$, that are associated with P-O or Si-O bonds. However, for x > 0, peaks grow in with added oxygen between 800 cm^{-1} and 1200 cm^{-1} .

The low intensity peak centered at 458 cm^{-1} for the x = 0 glass is assigned to BS bonds, i.e. Si-S-Si, P-S-P, and Si-S-P. As x increases, the intensity of this 458 cm^{-1} mode decreases and indicates that the BS bonds are being converted into NBSs when oxygen is incorporated. The

most significant peak at 587 cm⁻¹ is attributed to NBS vibrations in both Si-S⁻ and P-S⁻ SRO units. The larger proportion of NBS compared to BS is expected from this composition with its high, 0.56, mole fraction of Li₂S. To the high wavenumber side of this peak, the shoulder centered at ~720 cm⁻¹ intensifies with increasing x and is assigned to bending mode of Si-O-Si BOs. The intensity of this shoulder increases strongly from x = 0 to 0.33. In the higher wavenumber range, >800 cm⁻¹, of the spectra, there are peaks at 900 cm⁻¹, 965 cm⁻¹, and 1083 cm⁻¹ that are assigned to asymmetric stretching modes of the all oxide Si⁰, Si², and Si³ SRO units, respectively[52-58]

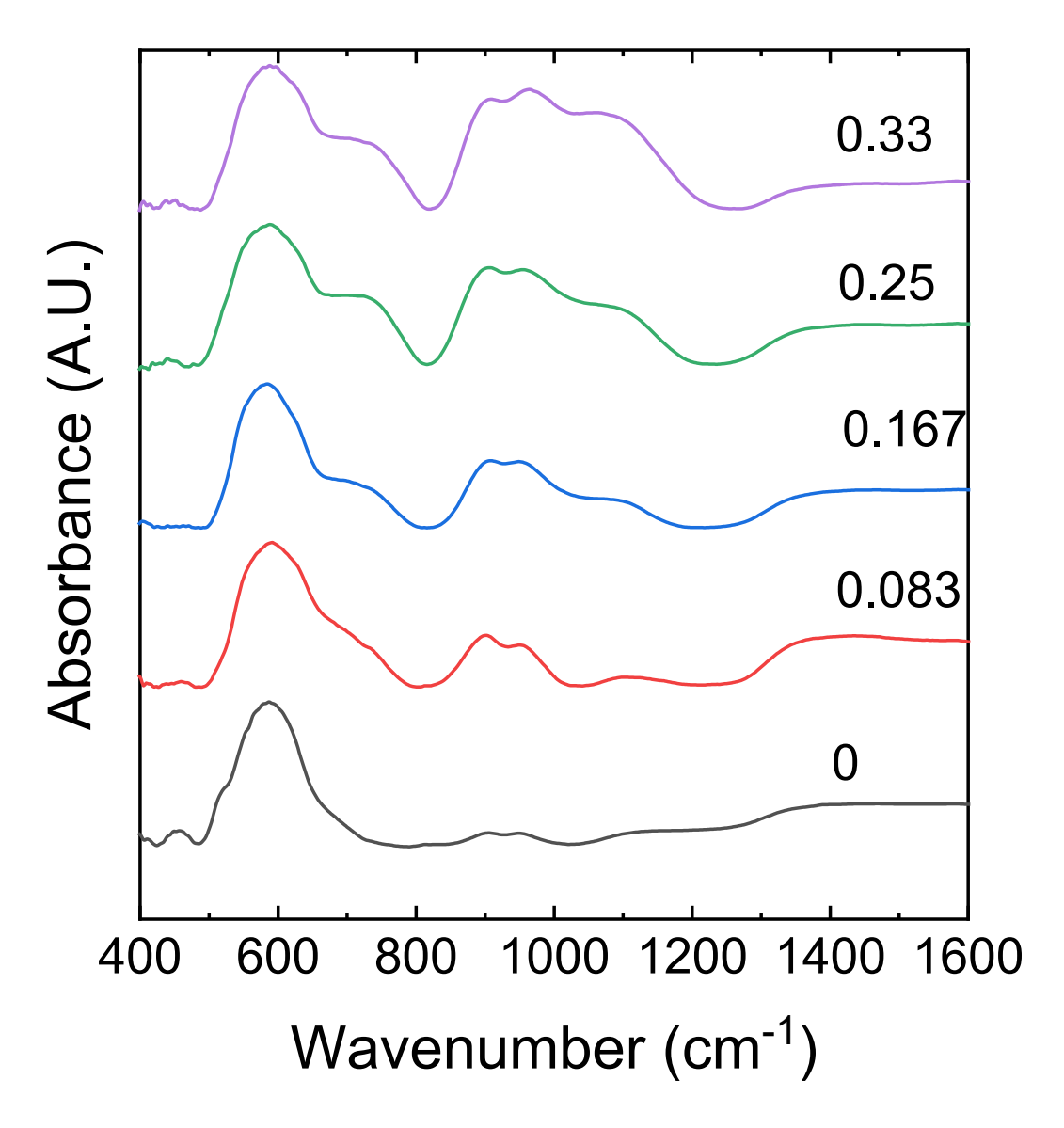


Fig. 5. High wavenumber range of Mid-IR spectra of $0.56\text{Li}_2\text{S} + 0.44[(0.33-x)PS_{5/2} + xPO_{5/2} + 0.67\text{SiS}_2]$ GSEs, x = 0, 0.083, 0.167, 0.25, 0.33.

3.5 MAS NMR Spectra

3.5.1 ³¹P MAS NMR Spectra

Since Si and P have similar SRO structures and atomic masses, it is hard to distinguish between the P-based and Si-based SRO structures using Raman and IR spectra alone. For this

reason, MAS NMR has been used as a powerful tool due to its selective sensitivity to different nuclei.

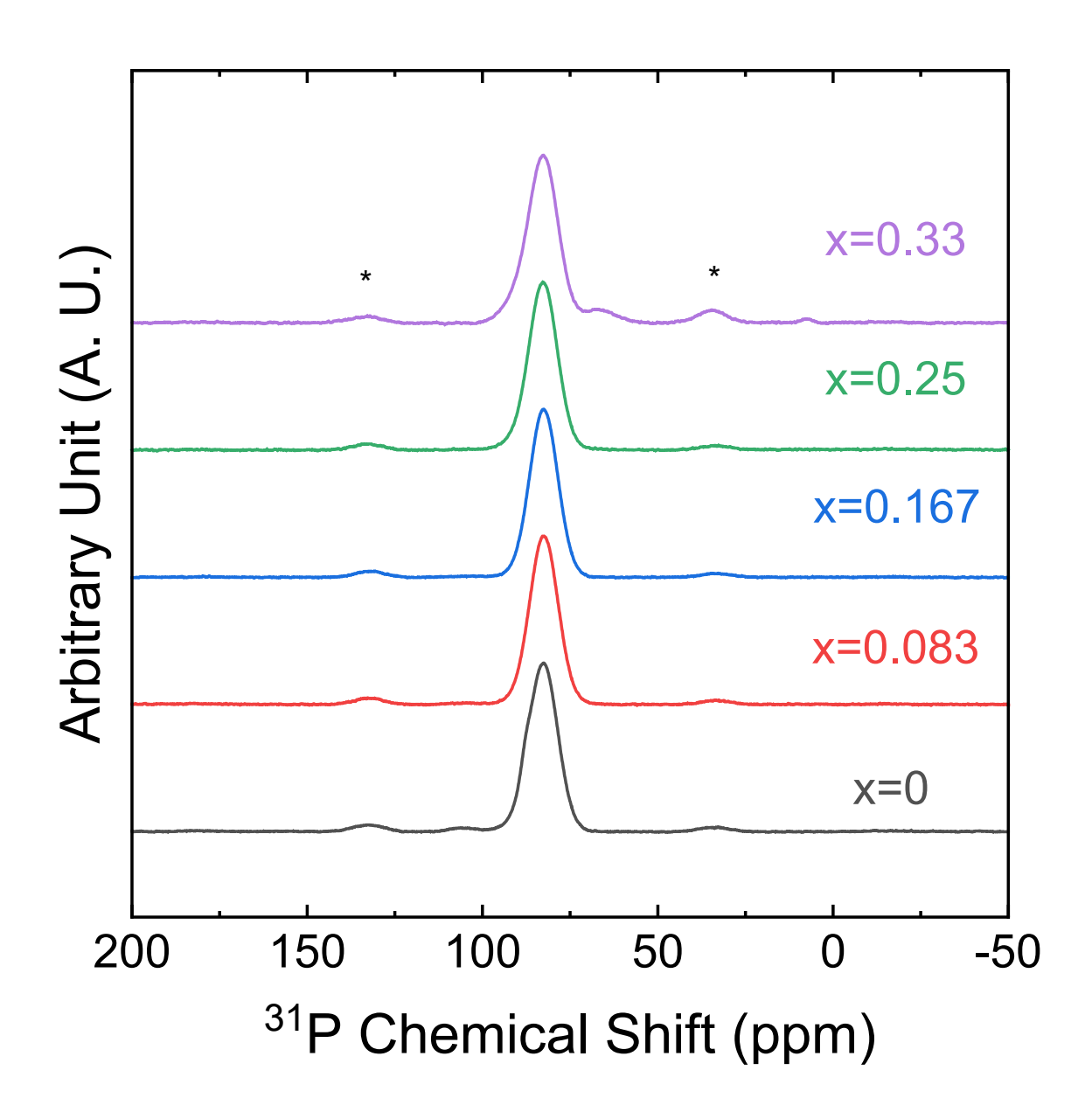


Fig. 6. ^{31}P MAS NMR spectra of $0.56Li_2S+0.44[(0.33-x)PS_{5/2}+xPO_{5/2}+0.67SiS_2]$ GSEs, x=0, 0.083, 0.167, 0.25, 0.33.

Figure 6 shows the ${}^{31}P$ MAS NMR spectra of all the GSEs in this series. There is only one major peak at ~83 ppm seen across all of these compositions. The weak spinning side bands are marked with asterisks,. This peak has been attributed to two kinds of P^0 units, PS_4^{3-} and PS_3O^{3-} . [27, 34, 59, 60] On careful inspection of this central peak, a small shoulder with a small positive chemical shift at 92-93 ppm is observed upon spectral deconvolution, see below, and has been assigned to the $P_2S_7^{4-}$, the pure sulfide P^1 , SRO unit. [40, 46] Due to these overlapping peaks, all of these spectra have been deconvoluted and examples of the end member GSEs, x = 0 and x = 0.33, are shown in **Fig. 7** and **Fig. 8**, respectively. All of the deconvoluted ${}^{31}P$ MAS NMR spectra are given in **Fig. S1** to **Fig. S5**. Table S1 provides all of the NMR fitting parameters used to arrive at these fits as well as the relative and relative and absolute fractions of these P SRO units for all of the GSEs studied in this work.

In addition to these two peaks, the GSEs with highest sulfur contents, x = 0 and 0.083, also showed a small peak centered at 104 ppm and it has been assigned to the P^{1P} unit. [40] This peak decreases in intensity, and therefore this SRO unit decreases in concentration, as more oxygen is incorporated and this behavior agrees with the observations made from the Raman spectra, **Fig. 4**, see above. [40] To the down field side of the main peak, a few very low intensity peaks emerge in the spectrum of the highest oxygen concentration sample, x = 0.33. These peaks are located at 65 ppm and 35 ppm and are assigned to the MOS P^0 SRO units $PS_2O_2^{3-}$ and the PSO_3^{3-} tetrahedral units, respectively. The peak for the MOS P^0 PSO $_3^{3-}$ SRO unit overlaps with a spinning side band from the main peak, but upon spectral deconvolution these two spectra features can be separated. There is also a very low intensity peak at 8 ppm which is assigned to the all oxide P^0 SRO unit, PO_4^{3-} . [27, 28, 34, 59, 60] The individual contributions of all of these P SROs to the overall P^0 MAS NMR spectra are shown in **Fig. 7** and **Fig. 8** for the P^0 and

0.33 GSEs, respectively. The composition, x, dependence of the relative and absolute fractional amounts of each of these P SRO units so determined from the ³¹P MAS NMR spectra are provided and discussed below.

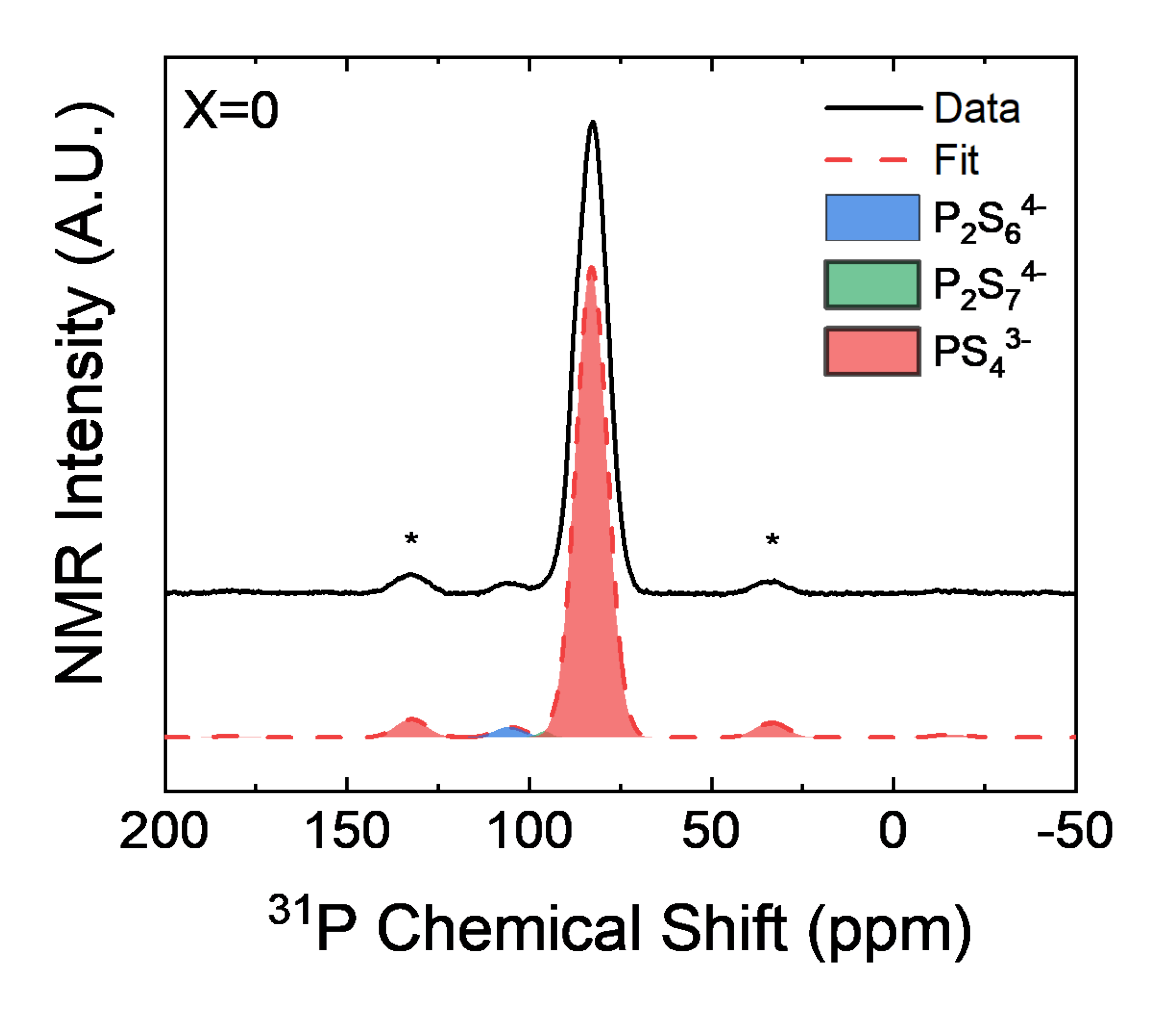


Fig. 7. ^{31}P MAS NMR spectra and deconvolution for the $x=0.0.56Li_2S+0.44[0.33PS_{5/2}+0.67SiS_2]$ GSE.

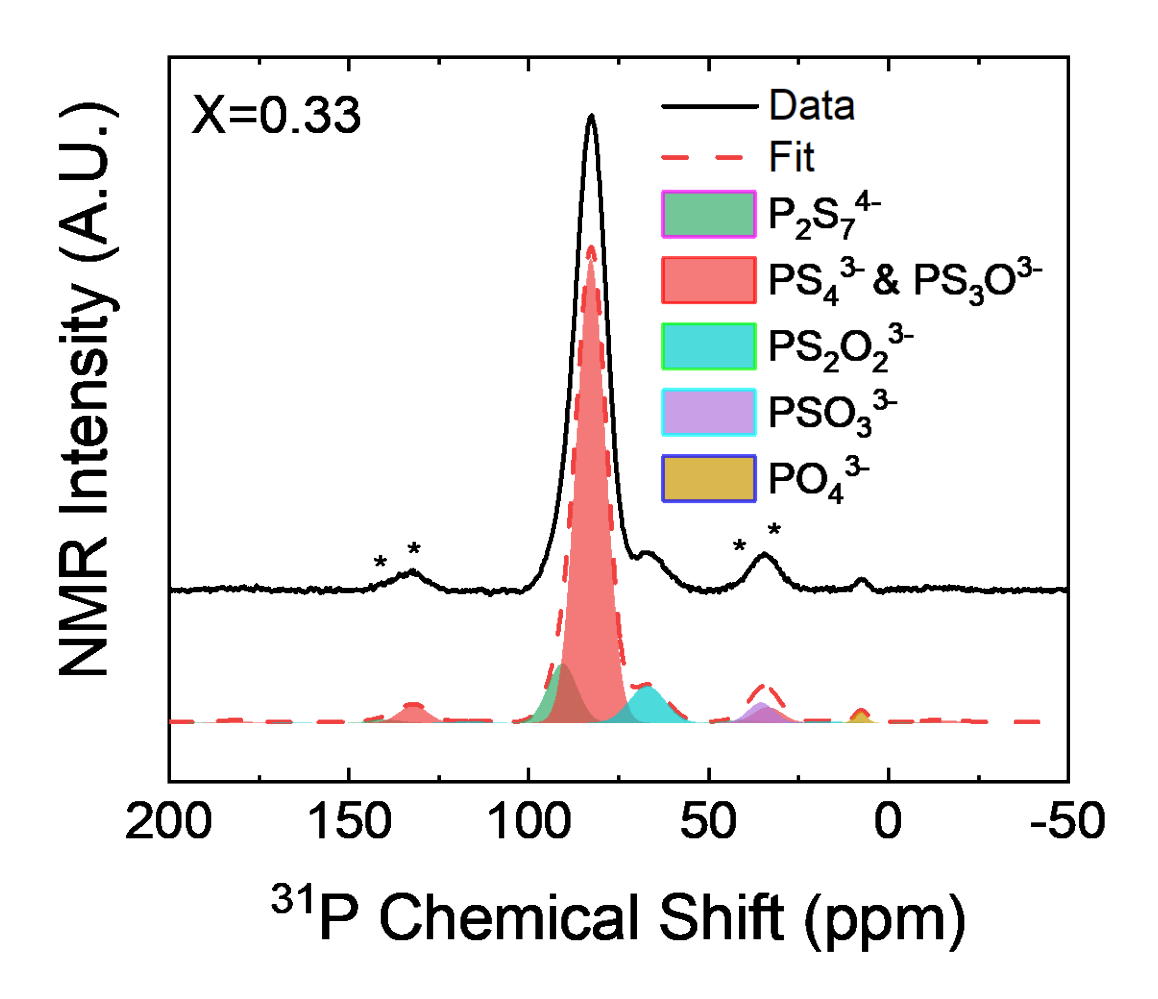


Fig. 8. ^{31}P MAS NMR spectra and deconvolution for the $x = 0.33~0.56Li_2S + 0.44[0.33PO_{5/2} + 0.67SiS_2]$ GSE.

3.5.2 ²⁹Si MAS NMR Spectra

Figure 9 gives the 29 Si MAS NMR spectra of 0.56Li₂S + 0.44[(0.33-x)PS_{5/2} + xPO_{5/2} + 0.67SiS₂] glass series. Due to the \sim 4% natural abundance of the 29 Si nuclide, the peaks in the Si MAS NMR spectra have significantly smaller S/N ratios than those in the 31 P MAS NMR spectra, even though the number of collected scans are far larger, \sim 10x larger, for the Si spectra.

This lack of high-quality spectra is common for Si bearing GSEs, but it does make analysis of the spectra more difficult.

For the x = 0 glass, there are only two major peak envelopes observed in the spectra. The first peak envelope on careful deconvolution, see **Fig. 10** and below, actually is comprised of four different absorption peaks, one centered at 2.75 ppm, and three centered -0.22 ppm, which are assigned to SiS₆⁶⁻ (Si^{1Si}) and the pure sulfide Si⁰, Si² and Si⁴, SRO units, respectively.[23, 61-63] On deconvolution, the peak at -0.22 ppm is found to be comprised of three equal contributions from the Si⁰, Si², and Si⁴ units with equal area and this has been accounted for in the charge balance of these GSE, see below.

Eckert et al. [23, 61-63] have performed a careful analysis of the SRO structures in alkali thiosilicate GSEs and has observed that multiple Si SROs have the same Si chemical shifts. They have found that the dominant effect changing the chemical shifts of the various Si SRO units is not the number of BS and NBS bonds on the silicon, like that seen in the alkali silicate glasses. Rather, they have found that the dominant effect is whether the Si unit has edge sharing bonding. There are two such edge sharing SROs possible, one where the Si shares a single edge, the E¹Si² SRO, nominally an Si² SRO, and one where the Si shares two edges, the E²Si⁴ SRO, nominally an Si⁴ SRO. The E₂Si⁴ unit is not observed in the GSEs studied here due to the high Li/(Si+P) ratio, 2.55, creating too many NBS in these glasses. However, the E¹Si² SRO unit is observed in these glasses in strikingly high concentration. This peak also exists in all of the compositions due to the high sulfur to oxygen ratio in the chemistry formula, 1 to 0.82. This is the first evidence in the Si NMR spectra of these glasses that suggests that the Si SRO units will be under-modified compared to P and relative to the Li/(Si+P)ratio of 2.55. That is, that the Si SRO units will have larger numbers of BO and BS than the composition of this series would suggest.

Returning to the 29 Si MAS NMR spectra of the x = 0 GSE, therefore, the second major peak centered at -11.20 ppm is assigned to the E^1 Si 2 SRO following the work above by Eckert et al. [23, 61-63]. This is further evidence that since this SRO unit corresponds to a nominal ratio of Li/Si of 0.5/0.5 = 1, the Si SRO units possess fewer Li $^+$ than the composition 0.56Li $_2$ S + 0.44[(0.33-x)PS $_{5/2}$ + xPO $_{5/2}$ + 0.67SiS $_2$] would suggest. This apparent disproportion of more Li $^+$ ions residing on the P SRO units than the Si SRO units is corroborated by the 31 P MAS NMR described above. The composition of this glass series would suggest that the P SRO units would consist of ~55% P 0 and 45% P 2 . Rather, as described above, the P SRO are essentially 90% P 0 and 10% P 1 .

Upon further inspection and deconvolution of the peak envelop in the chemical shift range of -3 to -12 ppm, four additional peaks that are observed are attributed to four new Si SRO units. The Si₂S₇³⁻ (Si¹) is observed at -3 ppm, the Si₂S₅¹⁻ (Si³) at -7.5 ppm, the molecular anion unt Si₄S₁₀⁴⁻ (Si^{3M}) at -9.5 ppm, and the Si₂S₆⁴⁻ (E¹Si²) at -10 to -12 ppm.[23, 61-63] Again, that the Si SRO units with higher numbers of BS are present than that suggested by the overall composition means that significant charge must have migrated to the P SRO units thereby creating larger and smaller numbers of NBS on P and Si, respectively, than the composition in this series would suggest. This is more fully discussed below.

Upon doping of these GSEs with $PO_{5/2}$, x > 0, see **Fig. 11** for the x = 0.33 GSE, the MOS SRO unit SiS_3O^{4-} is observed in the ²⁹Si NMR spectra and consistent with discussion above is located at the same chemical shift as the Si^4 , Si^2 , Si^0 SRO units.[23, 61-63] The addition of this Si^0 peak means that this peak at -0.22 ppm is actually comprised of four separate peaks, each with equal area. For the x = 0.083 to 0.33 GSEs, there are three other spectral regions which emerge and are located at -20 to -50 ppm, -55 to -90 ppm, and farther downfield at -90 to -115

ppm, These resonances have been attributed to SiS₂O₂⁴, SiSO₃⁴ and SiO₂ tetrahedra, respectively, with the Si⁰ units containing no bridging species and the SiO₂ being structured only with four BO, that is as an all oxide Si⁴ SRO unit. [26, 28-30, 60, 64, 65]

As seen in the 29 Si MAS NMR spectra and not observed in the 31 P MAS NMR spectra, there is an obvious trend for the formation of Si-O bonds with increasing x. This observation differs from the 31 P NMR spectra because the oxygen related structures are only observed in the 31 P MAS NMR spectra in very small intensity in the x = 0.33 glass. However, in the 29 Si MAS NMR spectra of the x = 0.33 GSE, there is significantly more spectral intensity associated with MOS and oxide Si SRO structures. This is consistent with the striking result that while oxygen is introduced in these GSEs as PO_{5/2}, essentially all of the oxygen is scavenged away from the P and becomes bonded to the Si.

The formation of preferential Si-O bonded species is consistent with the more negative $\Delta G^{o}_{formation}(SiO_{2}, 298K) = -205 \text{ kJ/mole}$ compared to that of $\Delta G^{o}_{formation}(PO_{5/2}, 298k) = -164 \text{ kJ/mole}$. However, it is noted that the formation and amounts of these different MOS SRO units are likely also dependent on other factors such as the $p(O_{2})$, melting temperatures, exact nature of the starting materials, etc. The fact that these free-energies of formations are consistent with the observations here suggests that these energies are at least one of the important factors in controlling which MOS species form in these glasses. The individual contributions of all of these SROs are shown in Fig. 12 and Fig. 13 for the phosphorus-based and silicon-based SRO units, respectively. The full deconvoluted spectra can be found in the SI in Fig. S6 – Fig. S10. Table S1 provides all the NMR fitting parameters used to arrive at these fits as well as the relative and absolute fractions of these Si SRO units for all of the GSEs studied in this work.

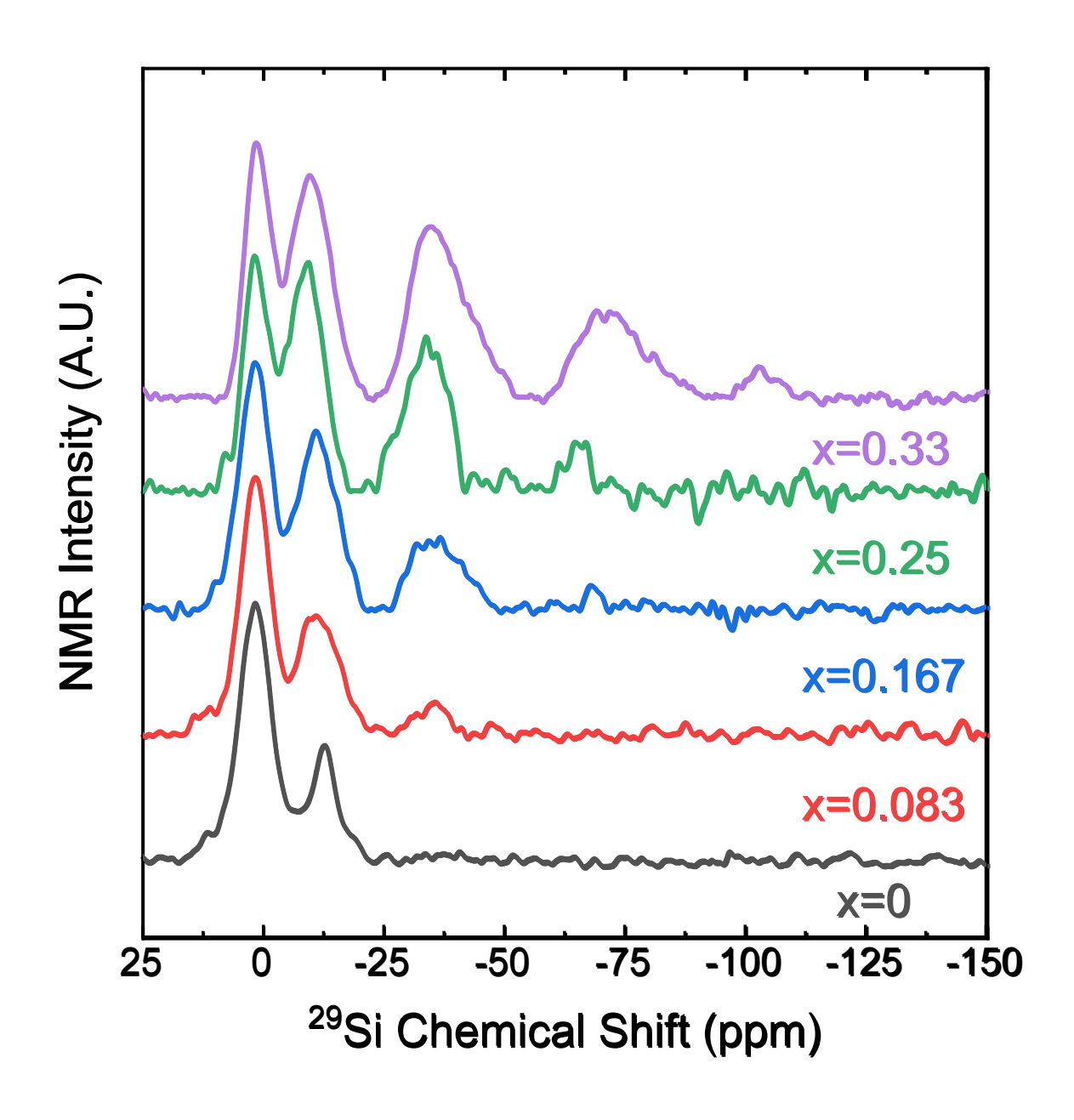


Fig. 9. ²⁹Si MAS NMR spectra of $0.56\text{Li}_2\text{S} + 0.44[(0.33-x)PS_{5/2} + xPO_{5/2} + 0.67\text{SiS}_2]$ GSEs, x = 0, 0.083, 0.167, 0.25, 0.33.

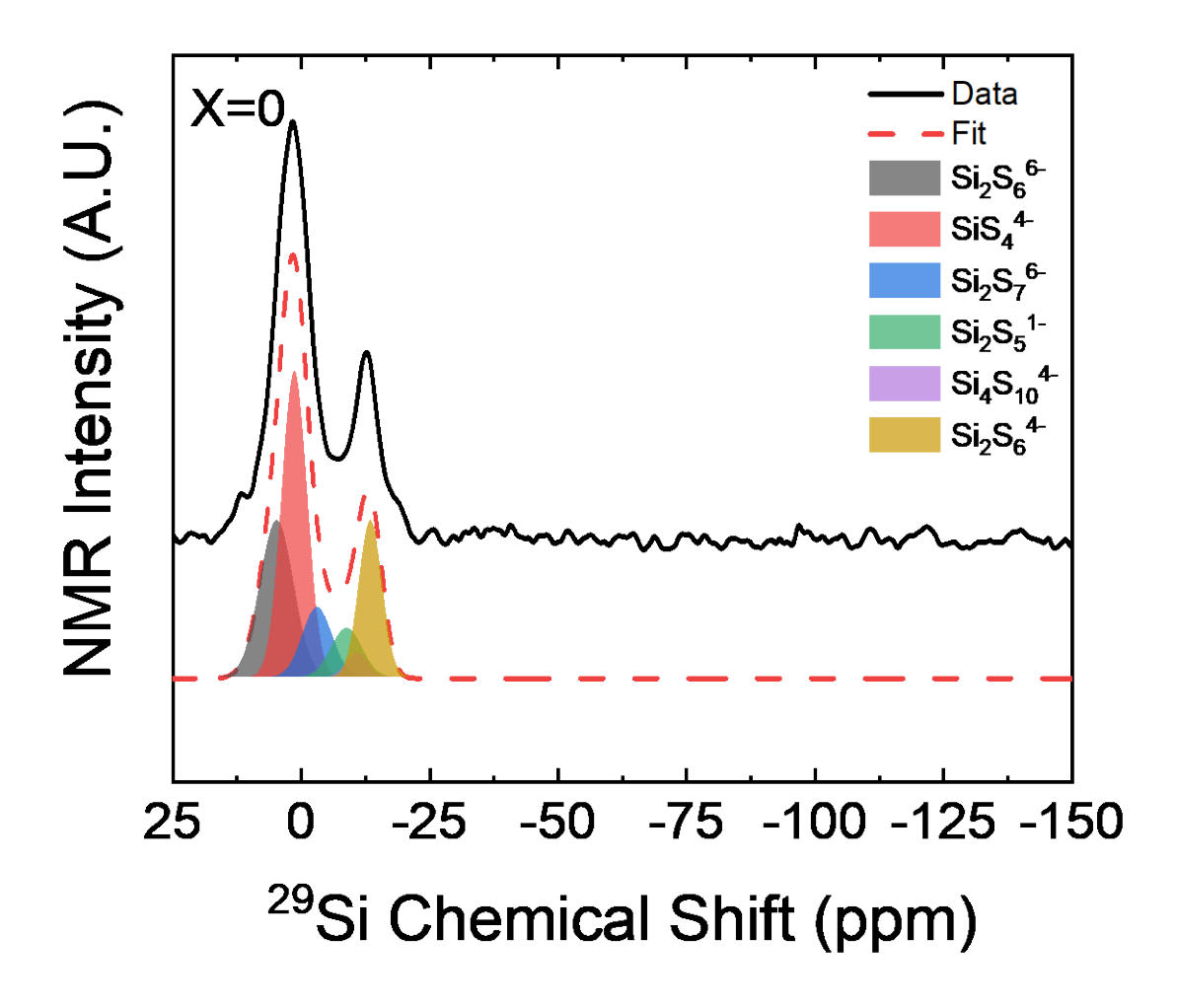


Fig. 10. ²⁹Si MAS NMR spectra and deconvolution for the $x = 0.0.56Li_2S + 0.44[0.33PS_{5/2} + 0.67SiS_2]$ GSE.

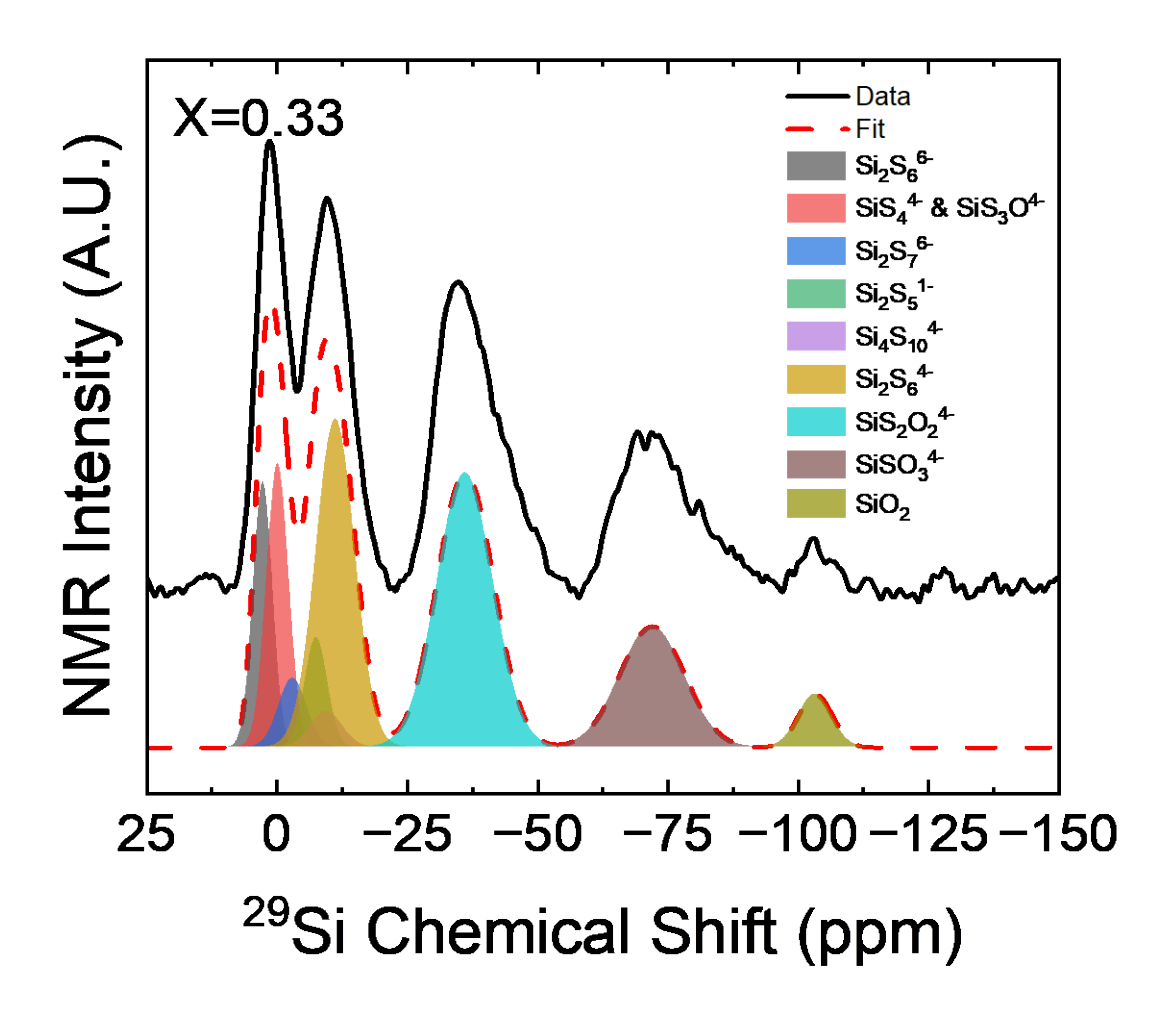


Fig. 11. 29 Si MAS NMR spectra and deconvolution for the $x = 0.33 \ 0.56Li_2S + 0.44[0.33PO_{5/2} + 0.67SiS_2]$ GSE.

4. Discussion

4.1 All Sulfide Glass

The x = 0 GSE is the only pure sulfide glass among all compositions within the composition series $0.56Li_2S + 0.44[(0.33-x)PS_{5/2} + xPO_{5/2} + 0.67SiS_2]$. Therefore, it has relatively different properties and SRO structural distributions than the other MOS GSEs in this series. First of all, it has lower Tg and Tc values than the MOS GSEs. **Fig. 2A** and **2B** show that

its Tg is 292 °C and its Tc is 384 °C, which are the lowest values among all compositions. This is expected as the sulfur anion has a larger radii and a smaller electronegativity in comparison to the oxygen anion, which is smaller and more electronegative. Therefore, the sulfide glass with its longer bond lengths and hence lower bond strengths allows the structure to deform and reconstruct with a smaller thermal energy.

Table 1. Glass transition (Tg) and crystallization (Tc) temperatures and working range $\Delta T \equiv Tc - Tg$ of the $0.56\text{Li}_2\text{S} + 0.44[(0.33-x)PS_{5/2} + xPO_{5/2} + 0.67\text{SiS}_2]$ GSEs.

Glass Composition (x)	Tg (°C)	Tc (°C)	$\Delta T \equiv Tc - Tg (^{\circ}C)$
0	292±2	384±5	95±7
0.083	300±3	407±4	110±7
0.167	309±3	403±4	97±7
0.25	324±3	405±3	84±6
0.33	315±4	414±6	102±10

Due to the nominal lack of oxygen in the x=0 glass, the ^{31}P and ^{29}Si MAS NMR spectra are dominated by all sulfide SRO structures. A less expected finding is that the ^{31}P MAS NMR spectra of the x=0 glass shows that this glass has more than 97% of sulfide P^0 unit and only about 3% of sulfide P^1 and P^{1P} units, see Table S1 and **Fig. 6** and **Fig. 7**.

Similar to the sodium thiosilicophosphate GSEs reported by Watson et al.,[48] the GSEs reported in this work also show a disproportionation between two glass formers. This structural disproportionation is the disproportionate sharing of the Li⁺ charges away from that expected where the average sharing of the charge held per Si and P unit is the same for P and Si in proportion to their relative amounts in the GSE. Here, as written in Eq. (1), for the Li/P ratio of

2.55, this glass would be expected to be comprised of 55% of P^0 unit, 45% of P^1 units and similarly 55% Si^1 and 45% Si^2 . The actual values for P and Si for the x=0 GSE, as described above and from Table S1, are 97% P^0 and 3% P^1 and 25.3% Si^{1Si} , 12.4% Si^0 , 12.4% Si^2 , 12.4% Si^4 , 10.0% Si^1 , 7.3% Si^{3M} , 2.6% Si^3 and 17.5% $E1Si^2$. This experimental observation confirms that disproportionation reactions occur during the synthesis process, where the P takes more charge, has more NBS, from Si and Si has less charge and hence more BSs and BOs, as shown in Eq (2). This indicates that P behaves as a disassociated dopant, and Si builds up the majority of the glass structure backbone.

Proportional Sharing of Charge:
$$\text{Li/P} = \text{Li/Si} = \text{Li/}(P + \text{Si}) = 2.55$$
 Eq. (1)

Disproportionate Sharing of Charge: $P^1 + Si^n \rightarrow P^0 + Si^{n+1}$ where n = 0, 1, 2, 3, 4 Eq. (2) In Eq. (2), n is the number of BS for the x = 0 pure sulfide GSE and the number of BS + BO in the x > 0 MOS GSEs.

4.2 Mixed Oxy-Sulfide GSEs

The addition of oxygen to the glass composition affects not only the distribution of the SRO structural species, creating BOs on Si and thereby forcing the formation of NBS on the P, it also effects the thermal properties. The Tgs and Tcs of the MOS GSEs increase with x, 300 to 325°C for Tgs and 400 to 415°C for Tcs, with a general increasing trend with increasing oxygen concentration. This means that the addition of oxygen enables these GSEs to have a larger supercooled liquid range which will benefit the potential application of these GSEs.

Similar to the pure sulfide glasses, the MOS glasses show a similar disproportionation reaction, but now the P and Si SRO units can also disproportionately exchange O and S and not just charge. In fact, it is found that all three, charge, oxygen, and sulfur are disproportionately shared. The percentage of P⁰ units, which includes all sulfide PS₄³⁻ SRO units and MOS PS₄₋

 $_yO_y^{3-}$ SRO units, where $0 \le y \le 4$, is higher than the expected value, 97 % versus 55%, across all of the MOS compositions. Therefore, a disproportionation reaction exists in all of the GSEs in this glass series. As shown in **Fig. 6**, all ^{31}P NMR spectra are similar except for the very small presence of the P^1 sulfide unit, i.e. $P_2S_7^{4-}$, and oxide and MOS P^0 units in the x=0.33 GSE as seen in **Fig. 7** and **Fig. 8**, respectively. Different from the ^{31}P NMR result, the ^{29}Si NMR spectra show noticeable changes and hence are indicative of very considerable differences in their various ^{29}Si SRO structures across the glass composition. Oxygen bearing Si SRO species appear even with a very minor addition of O doping, small x, as seen in **Fig. 10** and **Fig. 11**. The x=0.083 glass, for example, in which the O/(O+S) ratio is only 6%, shows a notable peak at around $^{-26}$ ppm, which is evidence of MOS Si^0 $SiS_2O_2^{4-}$ SRO units. As more oxygen is added, Si NMR peaks of all MOS SRO units increase noticeably with increasing O concentration and the overall MOS SRO species become the larger portion of the population of the silicon SRO structures.

Combined with the Raman and IR spectra, it can be concluded that by substituting $PS_{5/2}$ with $PO_{5/2}$ in this glass series, up to x=0.33, the P SRO structures remained almost constant, being dominated by the fully charged and depolymerized P^0 SRO sulfide units. The Si SRO structures, on the other hand, change dramatically. Even the oxygen atoms, having been introduced into the glass bonded to phosphorus from $PO_{5/2}$, showed great affinity to bond to Si over P during the glass melting process. The affinity of oxygen to silicon generates a variety of silicon MOS and oxide SRO structures which has been observed in all of the Raman, IR and NMR spectra of the MOS GSEs.

4.3 Quantitative Speciation of the P and S SRO Units

We now turn to quantitatively interpreting the ³¹P and ²⁹Si MAS NMR spectra by considering in detail the relative and absolute fractions of the various P and Si SRO units to

enable a better understanding of the local glass structure network in these GSEs. The net negative charge on the many and various P and Si SRO units can be determined from the deconvolution of ³¹P and ²⁹Si MAS NMR spectra. The net positive charge from lithium, +1.12, is fixed in this series and should equal the total net negative charge carried by all of the Si and P SRO units. This is shown in Eq (3).

Charge
$$/[P+Si] = -2.55 = \sum_{i=1}^{p} q_i f(P_i) + \sum_{j=1}^{s} q_j f(Si_j)$$
 Eq. (3)

In Eq. (3), q_i and q_j are the negative charges on the various P and Si SRO units, P_i and Si_j , respectively. For example, for the P⁰ SRO unit, $q_i = -3$ and $P_i = P^0$. The various fractions, $f(P_i)$ and $f(P_i)$ of the SRO units must sum to 1, namely that:

$$\sum_{i=1}^{p} f(P_i) + \sum_{i=1}^{s} f(Si_j) = 1$$
 Eq. (4)

All of the $f(P_i)$ and $f(P_j)$ values of all of the SRO units observed in these glasses were determined from the deconvolution of the P and Si MAS NMR spectra and were charge balanced to agree with Eq. (3). These values so determined are provided in Table S1 and are plotted in **Fig. 12** and **Fig. 13**, respectively.

Table 2.

Average negative charge per P and Si calculated by ³¹P MAS NMR and ²⁹Si MAS NMR deconvolution and charge compensation method using Eq. (3). Note that for proportional sharing the negative charge per P and Si should be the same and equal -2.55.

Glass Composition (x)	Negative Charge per P	Negative Charge per Si
0	-2.97	-2.26
0.083	-2.98	-2.26
0.167	-2.98	-2.26
0.25	-2.97	-2.27
0.33	-2.89	-2.30

Table 2 shows the average charge per glass former for all compositions in this series determined using Eq. (3) and the P and Si MAS NMR deconvolution data, provided in Table S1. The average negative charge on the Si SRO species ranges from -2.26 to -2.30 and the average negative charge on the P SRO species ranges from -2.89 to -2.98. These results agree with the Mid-IR spectra where Si-O-Si vibration modes arise from BO bearing Si SRO structures, i.e. Si² and Si³ SRO units.

Notably, the oxygen migration from P to Si observed in this glass series has not been observed in other MOS silico-phosphate GSEs.[26-30, 60, 64, 65] This could be a result of different starting materials and/or the modification extent of the GSEs, namely the Li/([P] +[Si]) ratio . All those reports use ionic Li₃PO₄ as the source of phosphorus and oxygen, whereas in this work covalent PO_{5/2} (P₂O₅) was used. Also, the GSEs in the works cited above have higher Li/([P] +[Si]) ratio, 3, than that of the GSEs reported here, 2.55 Li on average per glass forming atom in this work. This suggests that the oxygen exchange from P to Si during synthesis may more likely happen in the system with more networking sites.

The fractions $f_i(P_i)$ of all of the P SRO species in these GSEs are shown in **Fig. 12** and the fractions $f_i(Si_i)$ of all of the Si SRO species in these GSEs are shown in **Fig. 13**. As expected from the discussion above, there are dramatic differences between these sets of SRO populations. The P SRO are dominated by the pure sulfide P⁰ SRO, with only minor amounts of other pure sulfide and MOS SRO units. Hence the average charge on the P SRO units is \sim -3, as given in Table 2.

However, Fig. 13 shows that as expected from the discussion above, the composition dependence of the various fractions f_i of the Si SROs are very different. First and foremost, the Si SRO species are more numerous, 9 for Si versus 6 for P, and their fractions are more evenly distributed, whereas for P, the P⁰ SRO unit dominates for nearly all of the compositions. Next, as more oxygen is incorporated into the glass, the development of MOS SRO species becomes more prominent and there is a sharp reduction in the population of the pure sulfide species for Si. In particular, it is noted that the Si⁰ SRO unit with 2 NBOs, SiS₂O₂⁴, increases sharply while the pure sulfide Si⁰ SRO unit, SiS₄⁴⁻ decreases sharply. The high concentration of E¹Si² SRO units combined with the non-zero amounts of Si^2 and Si^3 units in the x=0 GSE pushes the average charge on the Si down below the -2.55 as expected from the composition of this GSE. As further oxygen is added, these more polymerized Si SRO units remain in the glass and the charge on the Si remains lower than -2.55. The sharp increase in the concentration of the E₁Si² SRO units combined with sharp decrease in the concentration of the Si¹ SRO units is in large part the cause of the lower than expected average charge on the Si SRO units. A graph showing all of the absolute fractions for all of the P and Si SRO species are shown in Fig. S11.

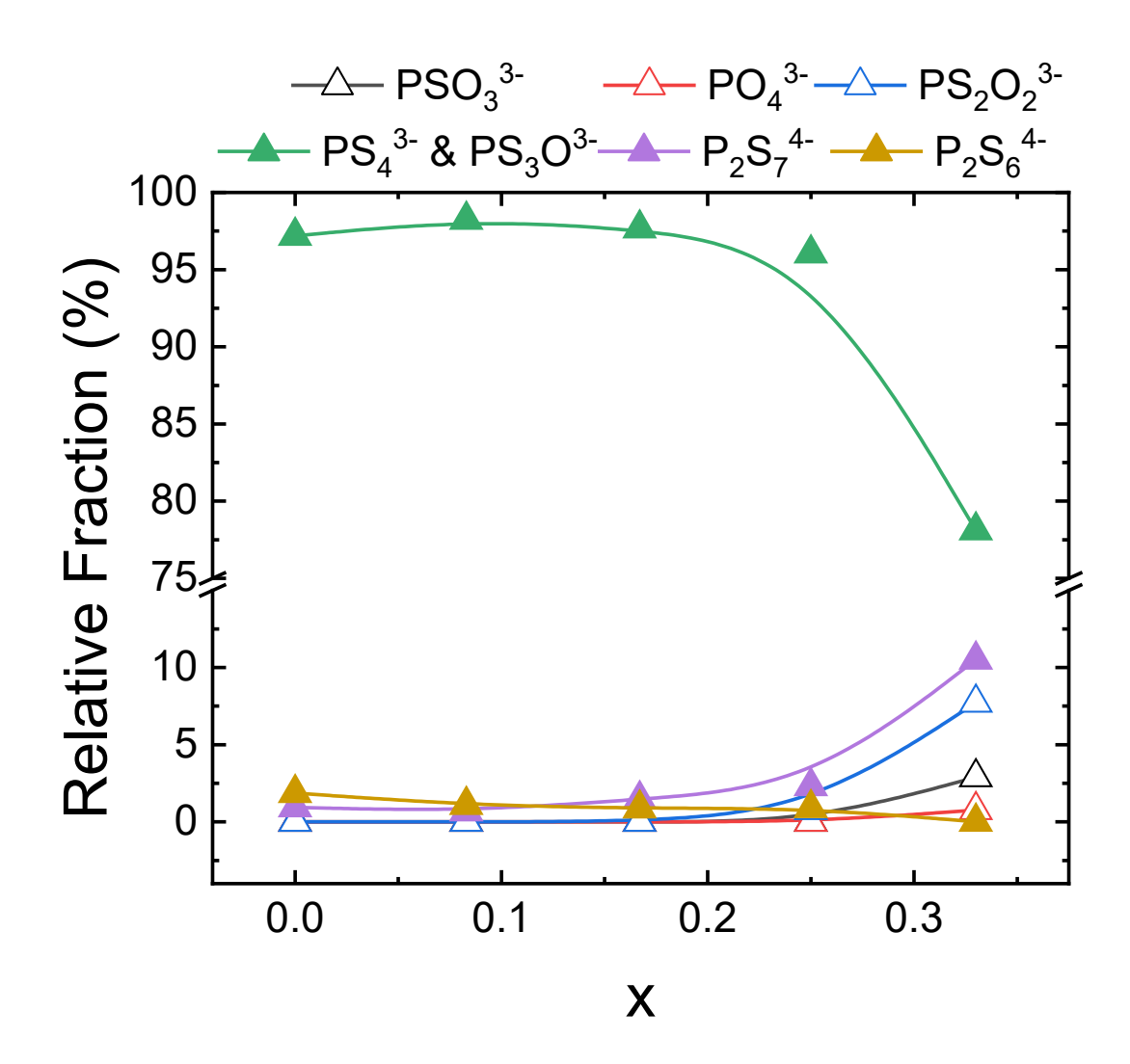


Fig. 12. Relative fractions of all of the P SRO units in $0.56\text{Li}_2\text{S} + 0.44[(0.33-x)\text{PS}_{5/2} + x\text{PO}_{5/2} + 0.67\text{SiS}_2]$ GSEs for x = 0, 0.083, 0.167, 0.25, 0.33. Note the broken scale on this graph that has been used to enable the very small fractions of the other P SRO units to be seen on this graph.

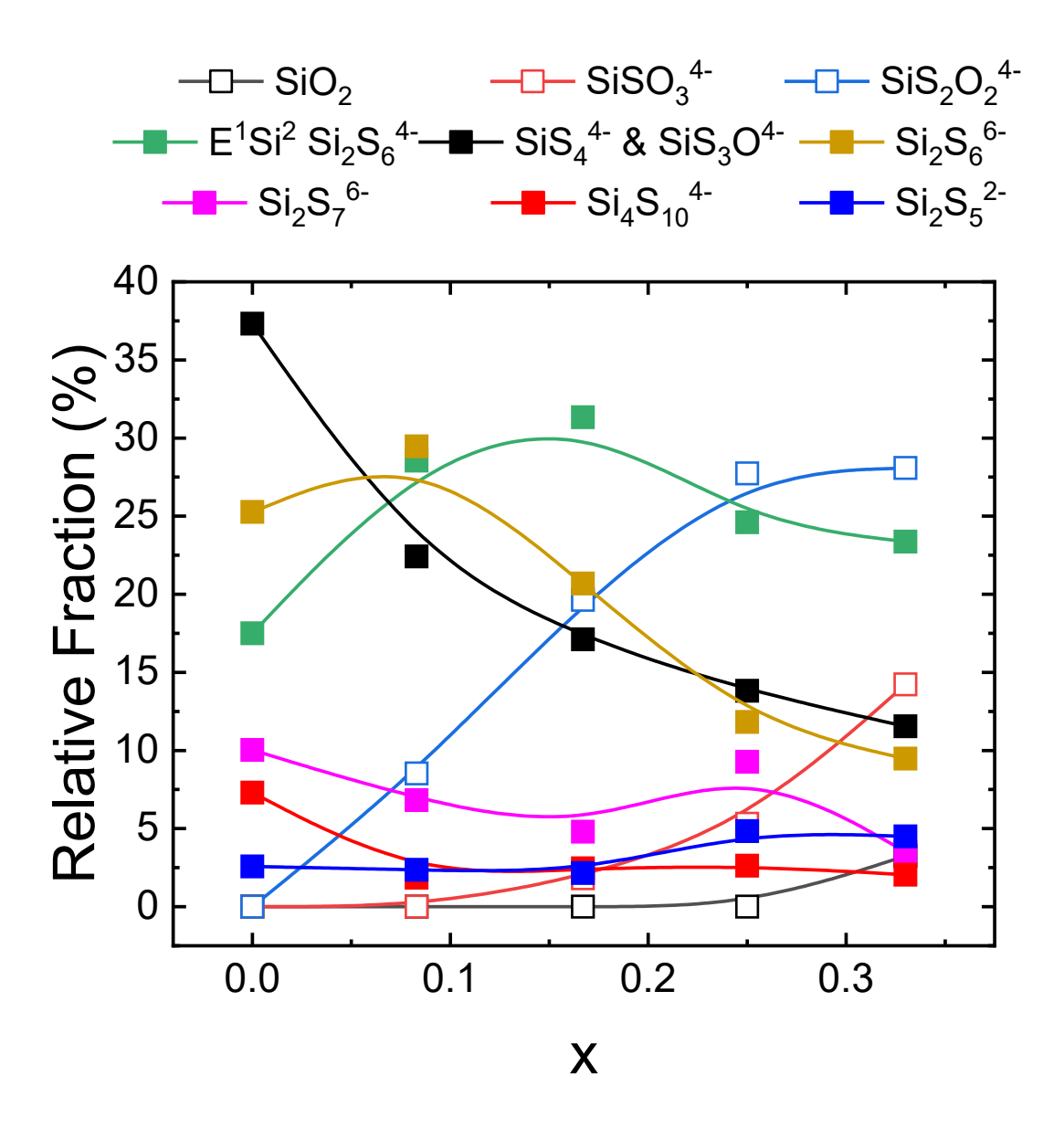


Fig. 13. Relative fractions of all of the Si SRO units in $0.56\text{Li}_2\text{S} + 0.44[(0.33-x)PS_{5/2} + xPO_{5/2} + 0.67\text{SiS}_2]$ GSEs for x = 0, 0.083, 0.167, 0.25, 0.33.

5. Conclusion

The glass composition series $0.56\text{Li}_2\text{S} + 0.44[(0.33-x)\text{PS}_{5/2} + x\text{PO}_{5/2} + 0.67\text{SiS}_2], x = 0,$ 0.083, 0.167, 0.25, 0.33 was synthesized using a melt-quench method in an open crucible inside

a N_2 -filled glovebox. The Tg and Tc temperatures were determined with DSC and it was observed that the MOS compositions, x > 0, have slightly higher Tgs and Tcs than the pure sulfide GSE, x = 0, showing a larger thermal stability window for SE applications. The atomic level structures of these GSEs have been analyzed using Raman, Mid-IR, and ^{31}P and ^{29}Si MAS NMR spectroscopies, and it is found that the P SRO structures exist mainly as the pure sulfide based and highly charged fully depolymerized P^0 units that have an average negative charge of -3.0. The Si SRO units are dominated by more covalent BO and BS structures that increase the average connectivity of the Si SRO units and lowers the overall average negative charge on the Si SRO units to about -2.3 from the compositionally expected value of -2.55. Further, there is essentially complete migration of O from oxygen bearing $PO_{5/2}$ species to sulfur bearing SiS_2 species. The observed higher oxygen anion affinity of silicon compared to phosphorus is consistent with the more negative free-energy of formation of Si-O species compared to that of P-O species.

Author declaration

We wish to confirm that there are no known conflicts of interest associated with this publication and there has been no significant financial support for this work that could have influenced its outcome. We confirm that the manuscript has been read and approved by all named authors and that there are no other persons who satisfied the criteria for authorship but are not listed. We further confirm that the order of authors listed in the manuscript has been approved by all of us. We confirm that we have given due consideration to the protection of intellectual property associated with this work and that there are no impediments to publication, including the timing of publication, with respect to intellectual property. In so doing we confirm that we have followed the regulations of our institutions concerning intellectual property.

We understand that the Corresponding Author is the sole contact for the Editorial process (including Editorial Manager and direct communications with the office). He/she is responsible for communicating with the other authors about progress, submissions of revisions and final approval of proofs. We confirm that we have provided a current, correct email address which is accessible by the Corresponding Author and which has been configured to accept email from swmartin@iastate.edu.

Declaration of Competing Interest

The authors declare that they have no known competing financial interests or personal relationships that could have appeared to influence the work reported in this paper.

Acknowledgement

The funding for this work was provided by the ARPA-E of Department of Energy through contracts numbered DE-AR0000778 and DE-EE0008852. Partial support of this work was also provided by the NSF through grants DMR-1936913 and DMR-2117445. The authors would like to thank Dr. Steven Kmiec, and Madison Olson of the Glass and Energy Materials Research Group, Dr. Sarah Cady of the ISU Chemistry Department Chemical Instrumentation Facility, and Professor Aaron Rossini of the Department of Chemistry for their assistance in collecting and analyzing the NMR spectra of these glasses. Finally, we would like to thank Stuart Leland of the Glass and Energy Materials Research Group for assistance in optimizing Fig. 1 in the paper.

References

- [1] B. Dunn, H. Kamath, J.-M. Tarascon, Science, 334 (2011) 928-935.
- [2] J. M. Tarascon, M. Armand, Nature, 414 (2001) 359-367.
- [3] P. G. Balakrishnan, R. Ramesh, T. Prem Kumar, Journal of Power Sources, 155 (2006) 401-414.
- [4] M. Nagao, A. Hayashi, M. Tatsumisago, T. Kanetsuku, T. Tsuda, S. Kuwabata, Phys Chem Phys, 15 (2013) 18600-18606.
- [5] X. B. Cheng, R. Zhang, C. Z. Zhao, Q. Zhang, Chem Rev, 117 (2017) 10403-10473.
- [6] J. P. Malugani, G. Robert, Solid State Ionics 1(1980) 519-523.
- [7] M. Ribes, B. Barrau, J. L. Souquet, Journal of Non-Crystalline Solids, 38-39 (1980) 271-276.
- [8] K. H. Kim, D. R. Torgeson, F. Borsa, J. P. Cho, S. W. Martin, I. Svare, G. Majer, J.Non-Cryst.Solids, 211 (1997) 112-125.
- [9] J. Kincs, S. W. Martin, Phys.Rev.Lett., 76 (1996) 70-73.
- [10] J. Cho, S. W. Martin, Ceramic Transactions, 65 (1996) 85-99.
- [11] I. Svare, F. Borsa, D. R. Torgeson, S. W. Martin, Phys.Rev.B: Condens.Matter, 48 (1993) 9336-9344.
- [12] H. K. Patel, S. W. Martin, Phys.Rev.B: Condens.Matter, 45 (1992) 10292-10300.
- [13] S. W. Martin, H. K. Patel, F. Borsa, D. Torgeson, Solid State Ionics, 53-56 (1992) 1141-1147.
- [14] S. W. Martin, H. K. Patel, F. Borsa, D. Torgeson, Journal of Non-Crystalline Solids, 131-133 (1991) 1041-1045.
- [15] S. W. Martin, D. R. Bloyer, T. Polewik, Ceram. Trans., 20 (1991) 147-159.
- [16] S. W. Martin, D. R. Bloyer, Journal of the American Ceramic Society, 74 (1991) 1003-1010.
- [17] S. W. Martin, J.Am.Ceram.Soc., 74 (1991) 1767-1784.
- [18] A. Pradel, M. Ribes, Materials Chemistry and Physics, 23 (1989) 121-142.
- [19] A. Hayashi, S. Hama, T. Minami, M. Tatsumisago, Electrochemistry Communications, 5 (2003) 111-114.
- [20] F. Mizuno, A. Hayashi, K. Tadanaga, M. Tatsumisago, Advanced Materials, 17 (2005) 918-921.
- [21] J. H. Kennedy, Y. Yang, J. Electrochem. Soc., (1986) 2437-2438.
- [22] A. Pradel, M. Ribes, Solid State Ionics, 18-19 (1986) 351-355.
- [23] J. H. Kennedy, Materials Chemistry and Physics, 23 (1989) 29-50.
- [24] R. Mercier, J.-P. Malugani, B. Fahys, G. Robert, Solid State Ionics, 5 (1981) 663-666.
- [25] A. Hayashi, M. Tatsumisago, T. Minami, Journal of The Electrochemical Society, 146 (1999) 3472-3475.
- [26] M. Tatsumisago, K. Hirai, T. Hirata, M. Takahashi, T. Minami, Solid State Ionics 86-88 (1996) 487-490.
- [27] K. Hirai, M. Tatsumisago, M. Takahashi, T. Minami, J Am Ceram Soc, 79 (1996) 549-552.
- [28] A. Hayashi, K. Tadanaga, M. Tatsumisago, T. Minami, Y. Miura, Journal of the Ceramic Society of Japan, 107 (1999) 510-516.
- [29] A. Hayashi, R. Komiya, M. Tatsumisago, T. Minam, Solid State Ionics, 152-153 (2002) 285-290.
- [30] A. Hayashi, H. Yamashita, M. Tatsumisago, T. Minami, Solid State Ionics, 148 (2002) 381-389.

- [31] M. Tatsumisago, K. Hirai, T. Minami, K. Takada, S. Kondo, Journal of the Ceramic Society of Japan, 101 (1993) 1315-1317.
- [32] Y. Kim, J. Saienga, S. W. Martin, J Phys Chem B, 110 (2006) 16318-16325.
- [33] Y. Kim, S. Martin, Solid State Ionics, 177 (2006) 2881-2887.
- [34] K. Minami, F. Mizuno, A. Hayashi, M. Tatsumisago, Journal of Non-Crystalline Solids, 354 (2008) 370-373.
- [35] A. Hayashi, H. Muramatsu, T. Ohtomo, S. Hama, M. Tatsumisago, Journal of Alloys and Compounds, 591 (2014) 247-250.
- [36] V. K. Deshpande, A. Pradel, M. Ribes, Mat. Res. Bull., 23 (1988) 379-394.
- [37] M. Yamashita, H. Yamanaka, H. Wakabayashi, Solid State Ionics, 89 (1996) 299-304.
- [38] M. Yamashita, H. Yamanaka, Solid State Ionics, 158 (2003) 151-156.
- [39] J. H. Kennedy, Z. Zhang, Solid State Ionics, 28–30 (1988) 726-728.
- [40] H. Eckert, Z. Zhang, J. H. Kennedy, Chem. Mater., 2 (1990) 273-279.
- [41] A. Pradel, C. Rau, D. Bittencourt, P. Armand, E. Philippot, M. Ribes, Chem. Mater., 10 (1998) 2162-2166.
- [42] C. Bischoff, K. Schuller, N. Dunlap, S. W. Martin, J Phys Chem B, 118 (2014) 1943-1953.
- [43] D. Massiot, F. Fayon, M. Capron, I. King, S. Le Calvé, B. Alonso, J. O. Durand, B. Bujoli, Z. Gan, G. Hoatson, Magnetic resonance in chemistry, 40 (2002) 70-76.
- [44] S. Kmiec, A. Joyce, S. W. Martin, Journal of Non-Crystalline Solids, 498 (2018) 177-189.
- [45] A. Pradel, M. Ribes, Journal of Solid State Chemistry, 96 (1992) 247-257.
- [46] K. Noi, A. Hayashi, M. Tatsumisago, Journal of Power Sources, 269 (2014) 260-265.
- [47] D. E. Watson, S. W. Martin, Journal of Non-Crystalline Solids, 471 (2017) 39-50.
- [48] D. E. Watson, S. W. Martin, Inorg Chem, 57 (2018) 72-81.
- [49] S. Kmiec, A. Joyce, D. Bayko, S. W. Martin, Journal of Non-Crystalline Solids, 534 (2020) 119776.
- [50] C. Bischoff, K. Schuller, M. Haynes, S. W. Martin, J. Non-Cryst. Solids, 358 (2012) 3216-3222.
- [51] M. Tachez, J.-P. Malugani, R. Mercier, G. Robert, Solid State Ionics, 14 (1984) 181-185.
- [52] O. N. Koroleva, M. V. Shtenberg, P. V. Khvorov, Russian Journal of Inorganic Chemistry, 59 (2014) 255-258.
- [53] J. J. Hudgens, S. W. Martin, J Am Ceram Soc, 76 (1993) 1691-1696.
- [54] J. Kapoutsis, E. I. Kamitsos, G. D. Chryssikos, Y. Yiannopoulos, M. Prassas, (2008).
- [55] F. Plascencia-Hernández, D. G. Araiza, H. Pfeiffer, Industrial & Engineering Chemistry Research, 61 (2022) 11012-11024.
- [56] A. Sanna, I. Ramli, M. M. Maroto-Valer, Energy Procedia, 63 (2014) 739-744.
- [57] M. Handke, Journal of Molecular Structure, 114 (1984) 187-190.
- [58] M. Handke, M. Sitarz, W. Mozgawa, Journal of Molecular Structure, 450 (1998) 229-238.
- [59] T. Ohtomo, A. Hayashi, M. Tatsumisago, K. Kawamoto, Journal of Non-Crystalline Solids, 364 (2013) 57-61.
- [60] A. Hayashi, R. Araki, K. Tadanaga, M. Tatsumisago, T. Minami, Phys Chem Glasses, 40 (1999) 140-145.
- [61] M. Tenhover, R. D. Boyer, R. S. Hendersoo, T. E. Hammond, G. A. Shreve, Solid State Communications, 65 (1988) 1517-1521.
- [62] H. Eckert, J. H. Kennedy, A. Pradel, M. Ribes, Journal of Non-Crystalline Solids 113 (1989) 287-293.
- [63] H. Eckert, Z. Zhang, J. H. Kennedy, Journal of Non-Crystalline Solids 107 (1989) 271-282.

[64] T. Minami, A. Hayashi, M. Tatsumisago, Solid State Ionics, 136-137 (2000) 1015-1023.[65] M. Tatsumisago, A. Hayashi, Journal of Non-Crystalline Solids, 354 (2008) 1411-1417.